

Fully Gapped s-wave-like Superconducting State and Electronic Structures in the $\text{Ir}_{0.95}\text{Pd}_{0.05}\text{Te}_2$ Single Crystals with Strong Spin-orbital Coupling

D. J. Yu,¹ F. Yang,¹ Lin Miao,¹ C. Q. Han,¹ Meng-Yu Yao,¹ Fengfeng Zhu,¹ Y. R. Song,¹ K. F. Zhang,¹ J. F. Ge,¹ X. Yao,¹ Z. Q. Zou,² Z. J. Li,³ B. Gao,³ D. D. Guan,¹ Canhua Liu,¹ C. L. Gao,^{1,*} Dong Qian,^{1,†} and Jin-feng Jia¹

¹Key Laboratory of Artificial Structures and Quantum Control (Ministry of Education),
Department of Physics and Astronomy, Shanghai Jiao Tong University, Shanghai 200240, China

²Center for Analysis and Testing, Shanghai Jiao Tong University, Shanghai 200240, China

³Shanghai Institute of Microsystem and Information Technology,
Chinese Academy of Sciences, Shanghai 200050, China

(Dated: September 24, 2018)

Due to the large spin-orbital coupling in the layered 5d-transition metal chalcogenides compound, the occurrence of superconductivity in doped $\text{Ir}_{2-x}\text{Pd}_x\text{Te}_2$ offers a good chance to search for possible topological superconducting states in this system. We did comprehensive studies on the superconducting properties and electronic structures of single crystalline $\text{Ir}_{0.95}\text{Pd}_{0.05}\text{Te}_2$ samples. The superconducting gap size, critical fields and coherence length along different directions were experimentally determined. Macroscopic bulk measurements and microscopic low temperature scanning tunneling spectroscopy results suggest that $\text{Ir}_{0.95}\text{Pd}_{0.05}\text{Te}_2$ possesses a BCS-like s-wave state. No sign of zero bias conductance peak were found in the vortex core at 0.4K.

As a new quantum state of matter, topological insulators (TIs) were theoretically proposed involving band inversion due to strong spin-orbital coupling (SOC) and experimentally discovered in compounds with high-Z elements such as HgTe, Bi-based compounds, Sb_2Te_3 ¹⁻⁷ and so on. Very soon after the discovery of TIs, extensive studies have been carried out in topological matters and topological phenomenon. One of the important topological states is so called topological superconductors (TSCs)^{2,8,9}, in which the zero-energy mode of Majorana Fermion that is proposed to be useful in topological quantum computation may harbor¹⁰. Previously, the most expected TSC is unconventional p-wave superconductor Sr_2RuO_4 ^{11,12}. After the conception of topological insulators, many effects for searching the possible TSCs have been put on the superconductors with large spin-orbital coupling. The possible candidates include Cu-intercalated topological insulator $\text{Cu}_x\text{Bi}_2\text{Se}_3$ ^{13,14}, In-doped SnTe ¹⁵ and so on. Some signs of zero energy conductance peaks that maybe related to Majorana Fermion were observed¹⁵⁻¹⁷. Recently, superconductivity was realized in a layered chalcogenide with high-Z elements: IrTe_2 with Pd, Pt and Cu¹⁸⁻²¹ substitution or intercalations. Because of the large SOC in this material, it becomes a possible candidate of TSC¹⁸. Though IrTe_2 is a layered compound, it is different from typical layered transitional metal dichalcogenides, IrTe_2 layers are bonded to each other by significant Te-Te bonding rather than weak Van der Waals force. IrTe_2 undergoes a structural phase transition from trigonal phase to triclinic phase at temperature of ~ 270 K^{18,22}. The origin of structure transition is still under debate. Fermi surface (FS) nesting, the Rice-Scott saddle-point mechanism, orbital-induced Peierls instability, crystal field effects, the interlayer hybridization states, the local bonding instability and the anionic depolymerization transition have been proposed²³. With intercalation or substitution at

the Ir sites of some nonmagnetic elements, the structural transition can be suppressed and bulk superconductivity is induced with T_c up to ~ 3 K. It'll be very interesting to know the details of superconducting state and how the electronic structures evolve in this system. In this letter, the superconducting properties and electronic structures in the $\text{Ir}_{0.95}\text{Pd}_{0.05}\text{Te}_2$ single crystals were studied by means of dc magnetic susceptibility, electrical resistance, band structure measurements and scanning tunnelling microscopy and spectroscopy (STM/STS) measurements. The superconducting gap size, coherence length, vortex states and band structures were experimentally determined directly. We find that $\text{Ir}_{0.95}\text{Pd}_{0.05}\text{Te}_2$ has a fully gapped weak-coupling BCS s-wave-like superconducting state and nearly identical low energy band structure as parent compound IrTe_2 . No zero bias conductance peak was detected in the vortex core, so topological superconducting state can be ruled out in this system at 0.4K.

High quality single crystals of $\text{Ir}_{0.95}\text{Pd}_{0.05}\text{Te}_2$ were grown using the chemical vapor transport method with iodine as a carrier agent. Doped samples were grown in a single step process in which iridium(99.99%), tellurium(99.999%), palladium(99.95%), and iodine powders (99.99%) according to the stoichiometric ratio were sealed in an evacuated fused silica ampoule. They were grown with a temperature gradient of 60°C with the hot end held at 880°C . The sample size is about $1\text{mm}\times 1\text{mm}\times 0.2\text{mm}$. As a comparison, parent compound IrTe_2 single crystals were grown out of Te flux using the same method as the previous works^{19,24}. The crystal structure was checked by x-ray diffraction (XRD) (Bruker) with Cu K_α line. The angle-resolved photoemission spectroscopy (ARPES) measurements were performed using 40 - 120 eV photons at Advanced Light Source beamlines 4.0.3 using Scienta R4000 analyzers with base pressures better than 5×10^{-11} torr. Energy

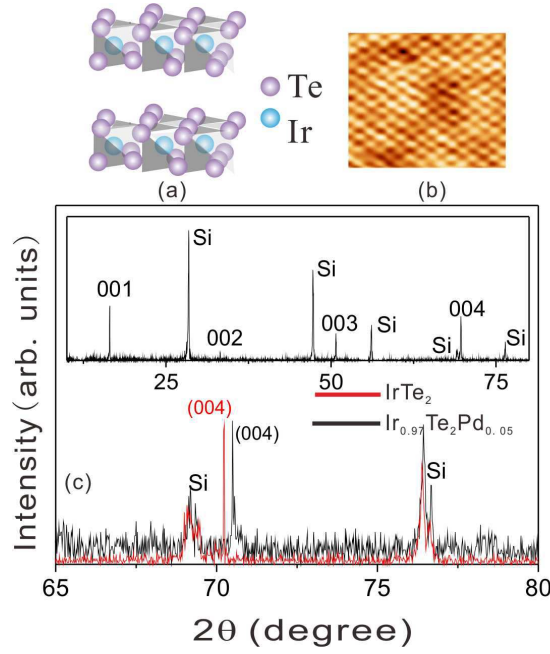


FIG. 1. (a) Sketch of the IrTe_2 crystal structure. (b) Atomic resolved STM image on the cleaving surface of $\text{Ir}_{0.95}\text{Pd}_{0.05}\text{Te}_2$ ($V=1.5$ V, $I=190$ pA). (c) XRD spectra of the single crystal $\text{Ir}_{0.95}\text{Pd}_{0.05}\text{Te}_2$ and IrTe_2 at (004) peak. The insert are the large range XRD spectra.

resolution is better than 15 meV and angular resolution is better than 0.02° . Low temperature STM/STS experiments were carried out in ultrahigh vacuum with a base pressure better than 1×10^{-10} Torr. Tungsten tips are used for STM/STS measurements. The dI/dV data of superconducting gaps were obtained via lock-in technique with modulation signal voltage 0.05 mV with a frequency of 985 Hz. The samples are cleaved in situ at 30K as well as at room temperature. The dc magnetization measurements were performed on a Quantum Design Physical Property Measurement System (PPMS). Temperature and magnetic fields dependent resistance measurements were carried out in the PPMS using the standard four-point probe technique with silver paste used for the contacts.

Figure 1 shows the crystal structure of IrTe_2 and the XRD spectra from the doped and the undoped crystals. Seen from Fig. 1(c), except the Si reference peak, all the diffraction peaks can be indexed by $(00l)$ peaks according to $P3m1$ structure from $\text{Ir}_{1-x}\text{Pd}_x\text{Te}_2$ with FWHM less than 0.05 degree which indicates the high crystalline quality of the samples. Si reference peaks were used to correct the system error. The (004) peaks were used to calculate the c-axis lattice constant. Based on Bragg condition, the calculated c-axis lattice constant is 5.386 Å and 5.372 Å for IrTe_2 and $\text{Ir}_{1.95}\text{Pd}_{0.05}\text{Te}_2$, respectively. After $x=0.05$ Pd doping, the lattice contracts by $\sim 0.26\%$ that is consistent with the Pd-Te substitution known from the powder samples¹⁸. After cleaving, the surface is Te-terminated. Fig. 1(b) shows well-ordered

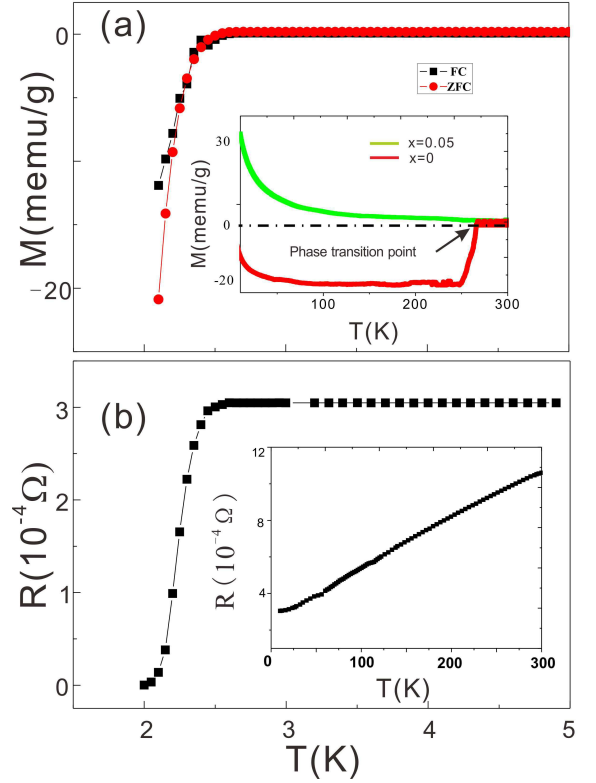


FIG. 2. (a) Temperature dependence of the dc magnetization under 20 Gauss field of $\text{Ir}_{0.95}\text{Pd}_{0.05}\text{Te}_2$ with zero field cooling (ZFC) and field cooled (FC). Diamagnetic signal is observed at ~ 2.5 K. Insert: Temperature dependence of the dc magnetization of $\text{Ir}_{0.95}\text{Pd}_{0.05}\text{Te}_2$ and IrTe_2 with 2T magnetic field applied perpendicular to the ab plane. (b) Temperature dependence of the resistance of $\text{Ir}_{0.95}\text{Pd}_{0.05}\text{Te}_2$ crystals with current flowing in the ab plane. Superconducting onset temperature is ~ 2.5 K. Insert: Temperature dependence of the resistance for $\text{Ir}_{0.95}\text{Pd}_{0.05}\text{Te}_2$ with 2T magnetic field applied perpendicular to the ab plane.

hexagonal lattice on the surface.

Typical low-temperature dc magnetic signal and electrical resistance of $\text{Ir}_{0.95}\text{Pd}_{0.05}\text{Te}_2$ samples are shown in Fig. 2. A diamagnetic behavior, characteristic of superconducting state, is observed below ~ 2.5 K. The magnetization signal obtained at 2.1 K is about 60% of that expected for full diamagnetism. This represents a conservative lower limit to the true superconducting volume fraction because the diamagnetic magnetization is still decreasing steeply at the temperature where the field is applied for the zero field cooling measurement. Figure 2b shows the temperature dependence of the resistance of $\text{Ir}_{0.95}\text{Pd}_{0.05}\text{Te}_2$, measured in the ab plane. Consistent with magnetic measurement, resistance of the sample decreases at ~ 2.5 K and reaches zero at ~ 2 K, suggesting bulk superconductivity. As presented in the insert of Fig. 2(a), with $x=0.05$ Pd substitution the magnetic signal increases monotonically in the doped samples with the decrease of temperature under the magnetic field of 2T.

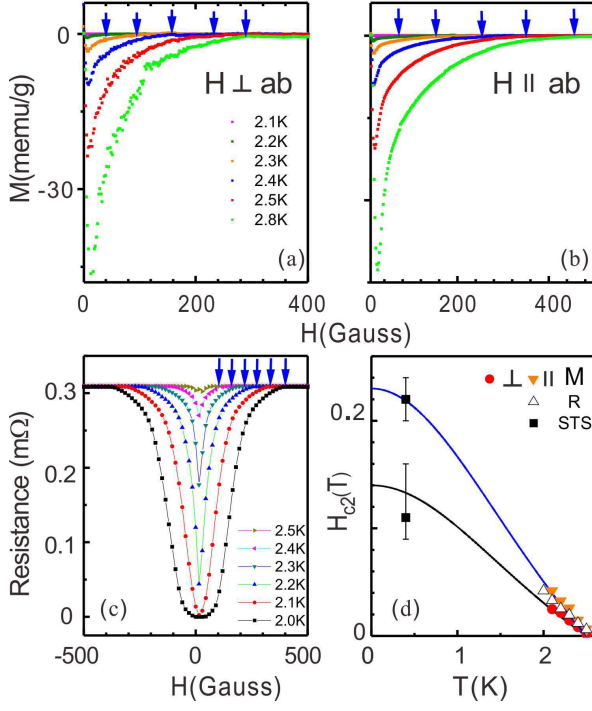


FIG. 3. $M(H)$ curves at $T = 2.1$ K, 2.2 K, 2.3 K, 2.4 K, 2.5 K and 2.8 K with magnetic field (a) perpendicular to ab plane. (b) parallel to ab plane. (c) Resistance as a function of magnetic field applied in ab plane at $T = 2.0$ K, 2.1 K, 2.2 K, 2.3 K, 2.4 K and 2.5 K. Blue arrows marking the position of $H_{c2}(T)$. (d) $H_{c2}(T)$ determined from $M(H)$, $R(H)$ and STS data at different temperatures. Solid curves are fitting curves to the magnetic signal measurements.

The structure phase transition is completely suppressed in $\text{Ir}_{0.95}\text{Pd}_{0.05}\text{Te}_2$, while IrTe_2 shows a sharp transition at $\sim 270\text{K}$ ¹⁸, marked by black arrow.

Detailed measurements of the magnetic signals and the resistance as a function of magnetic fields are presented in Fig. 3. Fig. 3(a) and (b) show the magnetization curves at different temperature (from 2.1K to 2.8K) along out-of-plane(\perp) and in-plane(\parallel) direction, respectively. Seen from the magnetization curves, $\text{Ir}_{0.95}\text{Pd}_{0.05}\text{Te}_2$ has typical type-II superconductor behavior. As shown in the Fig. 3(a,b), the blue arrows mark the position of $H_{c2\perp}$ and $H_{c2\parallel}$ where diamagnetic signals disappear at different temperature. In the resistance data (Fig. 3c), the upper critical field H_{c2} was defined at the superconducting onset temperature. Fig. 3(d) summaries the H_{c2} as a function of temperature. The linear temperature dependence close to T_c is obtained for H_{c2} , suggesting the dominance of only one type of bulk carrier, which is consistent with ARPES measurement shown below. The solid line is the fitting to Werthamer-Helfand-Hohenberg (WHH) theory based on the magnetic measurements. We obtained the upper critical field at zero temperature $H_{c2,\perp}(0) = 0.16 \pm 0.05$ T and $H_{c2,\parallel}(0) = 0.33 \pm 0.05$ T. From $H_{c2\perp}$, the coherence length $\xi_{\parallel} = \sqrt{\Phi_0/2\pi H_{c2\perp}} = 45\text{nm}$

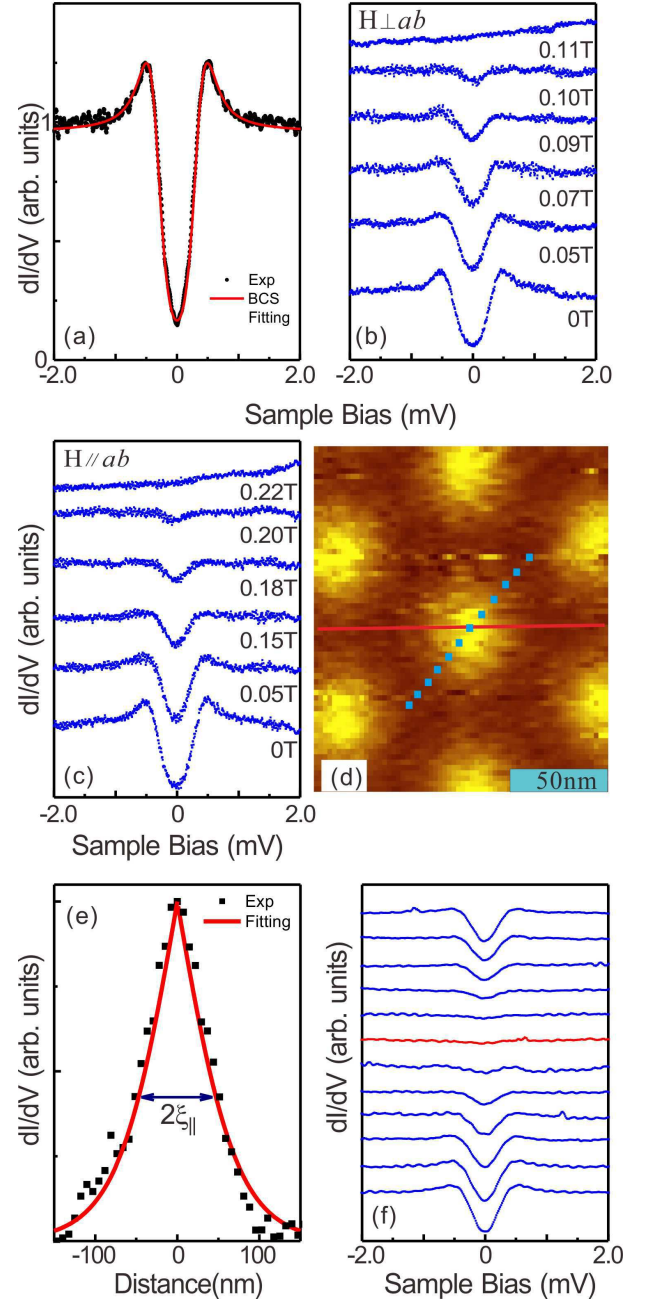


FIG. 4. (a) Typical superconducting gap (dI/dV spectra) measured at 0.4K . The distance between the tip and sample is set to be $\sim 1\text{nm}$. Superconducting gap is further confirmed by checking the evolution of the dI/dV spectra with magnetic fields (b) perpendicular to ab and (c) parallel to ab plane. (d) Superconducting vortex lattice measured by STS mapping. Applied magnetic field is 0.05 T. Red curve shows how to get the vortex's line profile. (e) Line profile of the single vortex. Red curve is the fitting curve to extract the coherence length. (f) dI/dV curves measured at different position according to blue dots in (d).

is obtained, while from $H_{c2\parallel}$ we use $\xi_{\parallel}\xi_{\perp} = \Phi_0/2\pi H_{c2\parallel}$ and obtain $\xi_{\perp} = 22nm$. So the dimensionless anisotropy parameter $\gamma = \xi_{\parallel}/\xi_{\perp} \sim 2$, which is smaller than another layered superconductor NbSe₂ ($\gamma \sim 3$).

The properties of the superconducting state are further explored by low temperature STM/STS. Fig. 4(a) shows the typical STS spectra obtained on the cleaved surface at 0.4K. Well-defined coherence peaks corresponding to the superconducting state was observed clearly. The STS spectra can be nicely fitted using BCS-type s-wave formula, which gives a superconducting gap of 0.36 ± 0.02 meV at 0.4K. Assuming the gap follows BCS theory, $\Delta(T) = \Delta(0)(1 - T/T_c)^{1/2}$, we get $\Delta(0) \sim 0.39 \pm 0.02$ meV, yielding the BCS ratio $2\Delta/k_B T_c \sim 3.6$. This value indicates a weak-coupling BCS-type superconductor (for weak coupling limit s-wave, BCS ratio ~ 3.5). The STS spectra as a function of applied magnetic fields are shown in Fig. 4(b) and 4(c). With the increase of applied magnetic field, the coherence peak faded away gradually. The energy gap disappears at about 0.11 T and 0.22 T when

magnetic field perpendicular or parallel to ab plane. It is worth noting that these two values are position dependent due to the existence of the vortex (vortices are shown in Fig. 4(d)) and the variation is much smaller when the magnetic field is applied in the ab plane. Nevertheless, the upper critical fields obtained in STS are well consistent with macroscopic bulk measurements as shown in Fig. 3(d). Superconducting vortex was observed by STS mapping. Fig. 4(d) shows the vortex with nice close-packed arrangement. From the size of the vortex, as shown in fig. 4(e), the in plane coherence length $\xi(T = 0.4K)$ of $\sim 51 \pm 5$ nm is obtained from the fitting of the line profile (red line in Fig. 4d) of the vortex, which is nearly consistent with the value from the bulk magnetic measurement. Small BCS ratio, s-wave-like gap function and long coherence length suggest that Ir_{0.95}Pd_{0.05}Te₂ is a fully gapped and weak coupling BCS-type s-wave superconductor. In addition, we carefully checked the STS at different position of vortex as shown in Fig. 4(f). Red curve in Fig. 4(f) is collected right at the center of a vortex. Outside the vortex, there is superconducting gap and gap closes at the center of the vortex. Under our experimental temperature (0.4K), no sign of zero bias conductance peak was observed at any position of vortex, which means even if there will be non-trivial superconducting states, much lower temperature is needed. From the STS measurement, we think we can rule out the possibility of topological superconducting state in this system at 0.4K.

Finally, the electronic structures of Ir_{0.95}Pd_{0.05}Te₂ are studied by ARPES. Same as IrTe₂, the energy bands of Ir_{0.95}Pd_{0.05}Te₂ show strong k_z dispersion. By tuning incident photon energy, we can change the detectable momentum along the normal direction (k_z). In-plane FS at different k_z was obtained by integrating the spectra weight with an energy window of 15 meV at Fermi energy. Changing of FS topology was observed in previous studies in IrTe₂ below and above the phase transition temperature^{23,25}. Fig. 5(a) shows the FS of Ir_{0.95}Pd_{0.05}Te₂ measured at 30K overlaid with the room temperature FS (green and blue dotted lines) of IrTe₂ from reference [24] at the exactly same k_z ($\sim 0.8\pi$) point using 90eV photon energy. Clearly, after Pd substitution, the FS of superconducting samples at low temperature is the same as that of IrTe₂ at room temperature. There are one outer big FS, three small Fermi pockets and a tiny Fermi pocket around zone center. Meanwhile, the three small Fermi pockets (blue dotted lines in Fig. 5-a) disappear at 30K in IrTe₂ samples²³. Fig. 5(c) and (d) show energy bands along the direction indicated by the yellow dotted lines in Fig. 5(a). Known from the band mapping, all the FSs are formed by hole-like bands. Since Ir_{0.95}Pd_{0.05}Te₂ has no phase transition but has identical FS as that of the IrTe₂ sample above phase transition temperature, it implies that itinerant origin such as FS nesting or saddle point nesting may not play key roles for the phase transition in this system. Phase transition is more likely related to local phenomena. For example, the

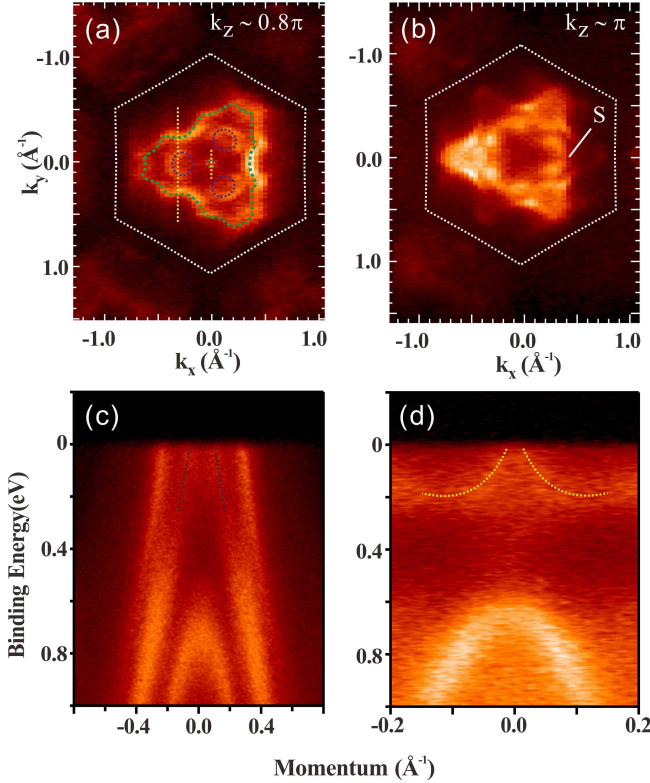


FIG. 5. (a) Fermi surface at $k_z \sim 0.8\pi$ on Ir_{0.95}Pd_{0.05}Te₂ measured at 30K. Green and blue dotted curves present the measured Fermi surface at room temperature on IrTe₂. No obvious different was observed between Ir_{0.95}Pd_{0.05}Te₂ and IrTe₂. (b) FS of Ir_{0.95}Pd_{0.05}Te₂ at $k_z \sim \pi$. "S" labels the same saddle point as in IrTe₂²³. (c) and (d) ARPES spectra at the momentum space as indicated in (a) by yellow dotted line. Black dotted line marks the hole-like bands crossing the Fermi level that sink beneath the Fermi level in IrTe₂ at low temperature.

depolymerization-polymerization of Te bonds was proposed to be involved in the phase transition²⁶. And it was also proposed that Ir 5d orbital reconstruction governed the charge and orbital instability in IrTe₂¹⁹. In addition, charge modulation originated from the periodic dimerization of Te atoms was observed in previous STM experiments²⁷. Fig. 5(b) presents the FS near π point. At this k_z point, saddle point (marked as "S" in the figure) observed in IrTe₂²³ remains in Ir_{0.95}Pd_{0.05}Te₂, which leave the possibility that the superconducting instability can be related to the van Hove singularity at saddle points²³. This scenario could be studied by ultra-low temperature ARPES experiments in the future.

In summary, we did comprehensive studies of the superconducting properties and electronic structures of Ir_{0.95}Pd_{0.05}Te₂. By combination of the macroscopic and microscopic measurements, the superconducting gap size, coherence length, electronics structures as well as the vortex states were determined. At 0.4K, the samples present a BCS-type s-wave-like superconducting behavior. Though no exotic superconducting state was found in this system, the hexagonal lattice structure of Ir_{0.95}Pd_{0.05}Te₂ is very suitable for epitaxially growth TIs. In our previous work, Bi₂Se₃ (Bi₂Te₃) TI films were

successfully grown on s-wave superconductor NbSe₂^{28,29}. This type of heterostructure utilizing the superconducting proximity effect perpendicular to the ab plane, so called vertical geometry. Superconducting Ir_{1-x}Pd_xTe₂ will be another excellent candidate for this geometry since its vertical coherence length is much larger than that of NbSe₂ ($\xi \sim 3$ nm). The heterostructure of TI/Ir_{1-x}Pd_xTe can be a good candidate for exploring topological superconductor related phenomena in the future.

This work is supported by National Basic Research Program of China (Grants No. 2012CB927401, 2011CB921902, 2013CB921902, 2011CB922200), NSFC (Grants No. 91021002, 10904090, 11174199, 11134008), the SCST, China (Grants No. 12JC1405300, 13QH1401500, 10JC1407100, 10PJ1405700, 11PJ405200). The Advanced Light Source is supported by the Director, Office of Science, Office of Basic Energy Sciences, of the US Department of Energy under Contract DE-AC02-05CH11231. D.Q. acknowledges additional supports from the Top-notch Young Talents Program and the Program for Professor of Special Appointment (Eastern Scholar) at Shanghai Institutions of Higher Learning.

* clgao@sjtu.edu.cn

† dqian@sjtu.edu.cn

- ¹ M. Z. Hasan and C. L. Kane, Rev. Mod. Phys. **82**, 3045 (2010).
- ² X.-L. Qi and S.-C. Zhang, Rev. Mod. Phys. **83**, 1057 (2011).
- ³ B. A. Bernevig, T. L. Hughes, and S.C. Zhang, Science **314**, 1757 (2006).
- ⁴ D. Hsieh, D. Qian, L. Wray, Y. Xia, Y. S. Hor, R.J. Cava and M.Z. Hasan, Nature **452**, 970 (2008).
- ⁵ Y. Xia, D. Qian, D. Hsieh, L. Wray, A. Pal, H. Lin, A. Bansil, D. Grauer, Y.S. Hor, R.J. Cava, M.Z. Hasan, Nature Phys. **5**, 398 (2009).
- ⁶ Y.L. Chen, J.-H. Chu, J.G. Analytis, Z.K. Liu, K. Igarashi, H.-H. Kuo, X.L. Qi, S.K. Mo, R.G. Moore, D.H. Lu, M. Hashimoto, T. Sasagawa, S.C. Zhang, I.R. Fisher, Z. Hussain, and Z.X. Shen, Science **325**, 178 (2009).
- ⁷ H.J. Zhang, C.X. Liu, X.L. Qi, X. Dai, Z. Fang, and S.C. Zhang, Nat. Phys. **5**, 438 (2009).
- ⁸ A. Schnyder, S. Ryu, A. Furusaki, A. Ludwig, Phys. Rev. B, **78**, 195125 (2008).
- ⁹ X.L. Qi, T.L. Hughes, S. Raghu, S.C. Zhang, Phys. Rev. Lett. **102**, 187001 (2009).
- ¹⁰ L. Fu, C. L. Kane, Phys. Rev. Lett. **100**, 096407 (2008).
- ¹¹ A. P. Mackenzie and Y. Maeno, Rev. Mod. Phys. **75**, 657 (2003).
- ¹² Y. Maeno, S. Kittaka, T. Nomura, S. Yonezawa, K. Ishida, J. Phys. Soc. J. **81**, 011009 (2012).
- ¹³ L. Fu and E. Berg, Phys. Rev. Lett. **105**, 097001 (2010).
- ¹⁴ L.A. Wray, S. Xu, Y. Xia, D. Qian, A.V. Fedorov, H. Lin, A. Bansil, L. Fu, Y.S. Hor, R.J. Cava, M.Z. Hasan, Phys. Rev. B, **83**, 224516 (2011).
- ¹⁵ S. Sasaki, Z. Ren, A. A. Taskin, K. Segawa, L. Fu, and Y.

- Ando, Phys. Rev. Lett. **109**, 217004 (2012).
- ¹⁶ S. Sasaki, M. Kriener, K. Segawa, K. Yada, Y. Tanaka, M. Sato, and Y. Ando, Phys. Rev. Lett. **107**, 217001 (2011).
- ¹⁷ V. Mourik, K. Zuo, S. M. Frolov, S. R. Plissard, E. P. A. M. Bakkers, L. P. Kouwenhoven, Science **336**, 6084 (2012).
- ¹⁸ J.J. Yang, Y. J. Choi, Y. S. Oh, A. Hogan, Y. Horibe, K. Kim, B. I. Min, and S.W. Cheong Phys. Rev. Lett. **108**, 116402 (2012).
- ¹⁹ D. Ootsuki, Y. Wakisaka, S. Pyon, K. Kudo, M. Nohara, M. Arita, H. Anzai, H. Namatame, M. Taniguchi, N.L. Saini, T. Mizokawa, Rev. B **86**, 014519 (2012).
- ²⁰ M. Kamitani, M. S. Bahramy, R. Arita, S. Seki, T. Arima, Y. Tokura, and S. Ishiwata, Phys. Rev. B **87**, 180501(R) (2013).
- ²¹ S.Y. Zhou, X.L. Li, B.Y. Pan, X. Qiu, J. Pan, X.C. Hong, Z. Zhang, A.F. Fang, N.L. Wang, S.Y. Li, EPL, **104**, 27010 (2013).
- ²² H.B. Cao, B.C. Chakoumakos, X. Chen, J.Q. Yan, M.A. McGuire, H. Yang, R. Custelcean, H.D. Zhou, D.J. Singh, D. Mandrus, Phys. Rev. B **88**, 115122 (2013).
- ²³ T. Qian, H. Miao, Z.J. Wang, X. Liu, X. Shi, Y.B. Huang, P. Zhang, N. Xu, P. Richard, M. Shi, M. H. Upton, J.P. Hill, G. Xu, X. Dai, Z. Fang, H.C. Lei, C. Petrovic, A.F. Fang, N.L. Wang, H. Ding, arXiv:1311.4946 (2013).
- ²⁴ A.F. Fang, G. Xu, T. Dong, P. Zheng, N. L. Wang, Sci. Rep., **3**, 1153 (2012).
- ²⁵ D. Ootsuki, S. Pyon, K. Kudo, M. Nohara, M. Horio, T. Yoshida, A. Fujimori, M. Arita, H. Anzai, H. Namatame, M. Taniguchi, N.L. Saini, T. Mizokawa, J. Phys. Soc. Jpn. **82** 093704 (2013).
- ²⁶ Y.S. Oh, J. J. Yang, Y. Horibe, and S. W. Cheong, Phys. Rev. Lett. **110**, 127209 (2013).
- ²⁷ P.J. Hsu, T. Maurer, M. Vogt, J.J. Yang, Y.S. Oh, S.W.

- Cheong, M. Bode, W.D. Wu, Phys. Rev. Lett., **111**, 266401 (2013).
- ²⁸ M.X. Wang, C.H. Liu, J.P. Xu, F. Yang, L. Miao, M.Y. Yao, C.L. Gao, C. Shen, X.C. Ma, X. Chen, Z.A. Xu, Y. Liu, S.C. Zhang, D. Qian, J.F. Jia, Q.K. Xue, Science **336**, 52 (2012).
- ²⁹ J.P. Xu, C.H. Liu, M.X. Wang, J.F. Ge, Z.L. Liu, X.J. Yang, Y. Chen, Y. Liu, Z.A. Xu, C.L. Gao, D. Qian, F.C. Zhang, Q.K. Xue, Jin-Feng Jia, arXiv:1312.3713 (2013).